RSC Advances

PAPER

View Article Online
View Journal | View Issue

Cite this: *RSC Adv.*, 2021, **11**, 5027

Structural, microstructural and magnetic characterization of the β-CoTe nanophase synthesized by a novel mechanochemical method†

Marcelo Augusto Malagutti,[a] Kelli de Fátima Ulbrich,[a] V. Z. C. Paes,[b] J. Geshev[b] and Carlos Eduardo Maduro de Campos *[a]

This work reports an unprecedented mechanochemistry synthesis of β-CoTe and its systematic characterization through X-ray powder diffraction (XRPD), transmission electron microscopy (TEM), and magnetometry techniques. The mechanical alloying produced the desired material within 6 h along with minor impurities, showing good stabilization for higher milling times (15 h) and long-term storage. XRPD characterization employed the Rietveld profile fitting analysis with fundamental parameters analysis in a direct convolution approach, giving the material's structure and microstructure information. For the spherical shape, the diameter mass average of the crystallites furnished values around 13 nm with 1.1% of microstrain. The double-Voigt procedure also modeled a triaxial ellipsoid shape for the crystallite size and obtained a surface-weighted average value for its volume around 150 nm^3. TEM images confirmed the nanometric size visually and showed the crystallites to aggregate in large particles hundreds of nanometers in size. Measuring hundreds of supposed crystallite sizes, we could achieve a numerical distribution of their sizes with an average of 16 nm. The magnetization analysis performed both experimentally and *via* numerical simulations showed that β-CoTe is predominantly superparamagnetic with a magnetic domain size compatible with the double-Voigt one.

Received 21st December 2020
Accepted 14th January 2021

DOI: 10.1039/d0ra10716f

rsc.li/rsc-advances

1. Introduction

The search for transition metal chalcogenides (TMC) materials' synthesis methods has drawn considerable attention during the last decades due to their broad application in material science. Their chemical and physical properties, enhanced by nanometric scale fabrication, make them suitable for applications in several areas of science like catalysis[1] (especially water electrocatalysis[2]), energy store and conversion,[3] solar cells,[4] and electronic devices.[5] Among the different types of synthesis methods, mechanochemistry has been in the ascendant in this decade. In this approach, mechanical energy through milling (shocks and shear from grinding/milling tools) can facilitate chemical reactions. Also, mechanochemistry is recognized to be a "green" method as it does not use solvents and its syntheses are performed in a controlled atmosphere near room temperature. Beyond that, the experimental procedures are easy and straightforward: their techniques apply material grinding to reduce sample grain sizes and augment homogeneity, increasing chemical activation. These procedures have been explored since the beginnings of human existence[6] and were shown to be of quite simple use until modern mechanical alloying techniques started to be developed in the 1960s.[7] TMCs have been explored by this method in many recent reports as reviewed by Baláž *et al.*[8]

TMC materials which have not been subject to mechanochemistry investigation include the Co–Te alloys, especially the β-CoTe phase (a hexagonal nickeline-type structure). Exploration of the phase diagram *via* mechanochemistry has not yet been reported and is our current objective for the 1 : 1 stoichiometry. The calculation of the phase diagrams method (CALPHAD) has recently been used to perform its thermodynamic assessment using available experimental data in the literature[9] from other synthesis methods. The β-CoTe phase and γ-$CoTe_2$ phase (marcasite-type) are described in this diagram, although the 1 : 2 stoichiometry presents a polymorphism with the pyrite[10] and $BaSi_2$-type structures.[11] The β-CoTe materials proved to have a homogeneity range from 55.4–64.2 at% Te at high temperatures, this wide range is explained by the Co vacancy defect mechanism, which adds another term for Co-vacancies' interactions in the grand partition function and corrects the phase diagram.[12] All these phases present a eutectic solid–liquid phase transition at a temperature of about 1288 K.

In the literature, the β-CoTe phases featured one of the lowest chemical shifts of the TMCs and the lowest effective-

[a]*Departamento de Física, Universidade Federal de Santa Catarina, 88040-970 Florianópolis, Brazil. E-mail: carlos.campos@ufsc.br*

[b]*Instituto de Física, Universidade Federal do Rio Grande do Sul, Porto Alegre 91501-970, Rio Grande do Sul, Brazil*

† Electronic supplementary information (ESI) available. See DOI: 10.1039/d0ra10716f

charge for Co. The inter- and intra-binding of Te–Te is short and furnished a low c/a ratio for the hexagonal cells.[13] The Seebeck coefficient is negative, also presenting a Curie–Weiss-like behavior for magnetic susceptibility[14,15] at high temperatures and hard ferrimagnetism at temperatures below 40 K. All these properties came from thermal synthesized materials,[11,16] in almost perfect bulk single crystals.

Due to these properties, the β-CoTe phase produced by solvothermal routes has been applied for biomolecular detection devices and has detected uric acid and adenine in human purine, which can indicate symptoms of diseases like gout and Parkinson's when in excess.[17] The properties which had the most influence were the good conductivity of these materials and the quantum confinement effect due to their size. Similar TMC materials, regarding their composition, have already been tested for biomolecular detection devices by this research group, examples are $NiTe_2$ for morin detection[18] and $Ni_{3-x}Te_2$ applied to dopamine and adrenaline detection,[19] all produced *via* mechanochemistry. So, the exploration of β-CoTe for these applications could be possible in the future. The phase is also considered a semiconductor with a band gap equal to 2.05 eV, which made viable the photo-reduction process using this phase and visible light to convert carbon dioxide into methane, showing its applicability for air cleaning.[20]

Many techniques can produce better quality nanostructures but are often more complicated and high cost (*e.g.* exfoliation and ion milling[21]). Mechanochemistry, in this regard, offers a good alternative to lower production costs since it involves a single-step procedure (the milling) to react the initial reagents with a great difference in melting points, it does not use toxic catalytic materials as solvothermal routes do, and it can be easily scaled-up by bigger millers.[8]

For these reasons of applicability and ease of synthesis, a novel synthesis of the β-CoTe phase through a mechanochemistry route, produced in a single-step procedure, is reported in this article. Here, pure elementary powders of Co and Te were used as the reagents in high-energy ball milling at room temperature and in an Ar atmosphere. The characterization procedures employed were X-ray powder diffraction (XRPD) and transmission electron microscopy (TEM), together with magnetic characterization through hysteresis loops, field cooling (FC), and zero field cooling (ZFC) measurements. Rietveld analysis was employed for XRPD *via* a direct convolution approach, fitting the peak profile with a conventional fundamental parameter approach (FPA) to obtain structural and microstructural information about the nanomaterial. Also, a double-Voigt (DV)[22] approach retrieved information about crystallite size (CS) anisotropy, showing an effective triaxial ellipsoidal modeling for the shape. All these analyses employed the total pattern analysis solution (TOPAS) software.[23] TEM allowed the counting of the visualized crystallites, showing a number average crystallite distribution. Our magnetization analysis, both experimental and through numerical simulations, allowed the determination of certain ferromagnetic and superparamagnetic characteristics of our samples.

2. Experimental section

2.1. Synthesis

The reagents used in the synthesis were elementary micrometric powders: Co (Sigma-Aldrich, 99.9+% purity) and Te (Sigma-Aldrich 99.99% purity). These elements were mixed in a vial with 65 mL capacity in the atomic proportion of 1 : 1, together with nine steel balls: three of 12.7 mm of diameter and six of 6.35 mm. The total mass used as the reagent was 3.1 g with a ball-to-powder ratio (BPR) equal to 10 : 1. The mechanochemical synthesis was performed in a High Energy Ball Mill SPEX 8000, using 1425 cycles a minute. All the preparation was realized in an Ar atmosphere to avoid oxidation. For every 3 h of milling time, about 0.100 mg of the material was fished out and stored in microtubes of 2 mL each for further characterization procedures. These are the standard parameters and procedures when dealing with TMCs in our lab, as can be seen in our recent publications,[24–26] hence they are used for this synthesis as well.

A second batch was produced and confirmed the reproducibility of the synthesis. All the samples studied were stored from the day of their synthesis up to about 300 days (>10 months) in small plastic microtubes closed to the air and kept at room temperature (RT). The samples were regularly re-examined by XRPD and the results attested to their long-term storing stability.

2.2. Characterization

Five techniques were implemented for the materials characterization: XRPD, selected area electron diffraction (SAED), imaging by TEM, vibrating sample magnetometry (VSM), and the physical properties measurement system (PPMS). The conventional Rietveld method was used to perform XRPD data analysis with the DV approach in the TOPAS software.

2.2.1. X-ray powder diffraction. The Panalytical X'pert Pro X-ray diffraction system was responsible for XRPD laboratory measurements using a Bragg–Brentano reflection geometry. In it, the powder material was placed in a zero-background silicon sample holder with dimensions of 16 mm in diameter and 0.2 mm in depth. The X-ray source was an ordinary Cu target tube with generator settings of 45 kV and 40 mA. The system optics used Soller slits of 0.04 mm, which were present in the incident and diffracted beams. The anti-scatter and divergent slits used were of 1° and 0.5° in angular size, respectively. A graphite monochromator reduced the K_β radiation and was placed at the diffracted beam to prevent fluorescent radiation. The X'Celerator RTMS detector was responsible for collecting the output signal. Generally, the room temperature measurements took five scans from 10° to 150° in 2θ with steps of 0.5° for each 240 s. The use of a knife reduced the air scattering contribution but decreased the maximum range of data collection from 150° to 90° due to physical limitations.

The Rietveld analysis was accomplished by the TOPAS suite of programs, starting from structure models obtained in the ICSD Database.[27] The description of the background function used the Chebyshev 8th polynomial order. Lorentzian and Gaussian distributions modeled the phase peak profiles for CS

and microstrain (MS), respectively. These functions were convoluted with the experimental and emission profiles achieved by the simple axial mode and the Holzer K_α and K_β models,[28] respectively, which were retrieved by fitting measurements of a LaB_6 sample standard.[29] A DV approach calculated the CS anisotropy with the triaxial ellipsoid modeling using the TOPAS macro in the ref. 22. Thermal dislocation parameters used isotropic models for all the atoms, keeping atomic coordinates fixed.

2.2.2. Structural and microstructural XRPD analysis. Space group indexation occurred through a comparison of the experimental data with database information from the Inorganic Crystal Structure Database (ICSD).[27] A match was found with the hexagonal CoTe $P6_3/mmc$ (ICSD card number 53090) and the predominant phase. Unwanted phases matched as Co $P6_3/mmc$ (ICSD 44990), CoO $C12/m1$ (ICSD 17013), and Fe $Im\bar{3}m$ (ICSD 64998). The crystal information file (.cif) was inputted into TOPAS to refine the structure and to obtain the microstructural information. The crystal data of the sample milled for 15 h without a knife, using the FPA and the preceding space group furnished β-CoTe lattice parameters of $a = b = 3.8949(2)$ Å and $c = 5.3809(4)$ Å, a volume of 70.70(1) Å^3, a calculated density of 8.7642(9) g cm^{-3}, R_p and R_{wp} of 2.28% and 2.94% respectively, and a goodness of fit (GoF) of 1.80 from 1556 data points. The domain size mass average is 12.58(8) nm using a Lorentzian peak profile. The isotropic MS reached 1.1% ($e_0 = 0.2\%$), using a Gaussian peak profile and a Gaussian distribution for the deformations.

2.2.3. TEM, HRTEM and SAED. Imaging by TEM and SAED was carried out on a JEOL JEM-1011 machine with a maximum magnification of 600 000 times and 100 kV of electron acceleration voltage. JEMS[30] electron microscopy simulation software is responsible for the simulation of electron diffraction data using the refined structure obtained by Rietveld.

2.2.4. Magnetic measurements. The magnetization (M) hysteresis loop measurements were performed *via* a Microsense EV9 system with a magnetic field, H, ranging from −20 kOe to 20 kOe at 300 K with a sample mass of approximately 10 mg. Further measurements used a PPMS from Quantum Design Dynacool, measuring $M \times H$ curves with an amplified range from −40 kOe to 40 kOe at different temperatures, from 300 to 10 K. Magnetization behavior was obtained by using the ZFC/FC protocol with an applied magnetic field of 100 Oe.

3. Results and discussion

3.1. Structural and microstructural characterization

Fig. 1(a) shows the experimental XRPD patterns of the $Co_{50}Te_{50}$ samples obtained for different processing (milling) times. The majority phase corresponded to the β-CoTe accompanied by a tiny quantity of residuals of Co and CoO (unreacted materials) and Fe. Here one can observe that for 3 h of milling time, it is hard to identify any phase but after 6 h, β-CoTe peaks appeared and are notably the predominant phase in the material. Unfortunately, CoO presents a peak around 60° and Co appears near 45°, as seen in Fig. S1–S4 of the ESI.† Fe powder was detected after 12 h of milling and was caused by contamination

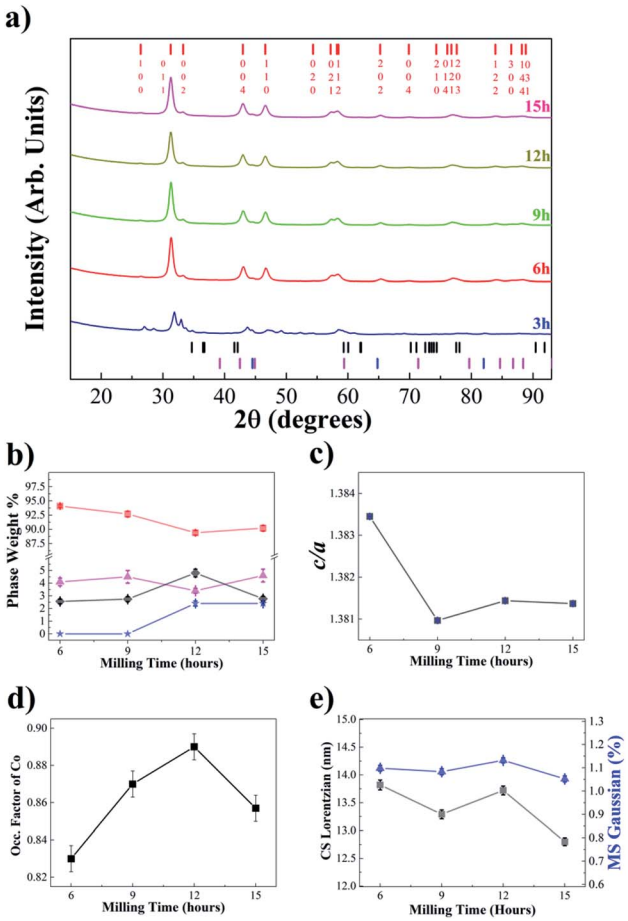

Fig. 1 (a) Diffractograms obtained by XRPD showing the samples' evolution with milling time. The tick markers represent the Bragg reflections, red stands for the β-CoTe, blue for Fe, magenta for Co, and black for CoO. No background subtraction was performed. (b) Phase weight percentages of the materials' elements against time. The colors represent the same phases from the previous graph ticks. The β-CoTe structural and microstructural parameters with milling time evolution. (c) Close-packing ratio evolution with time. (d) The occupational factor of the Co atom retrieved by Rietveld at different milling times. (e) Average crystallite size (black) and microstrain (blue) also obtained *via* TOPAS.

from the collisions of the balls with themselves and the recipient walls, generating wear of the milling tools and introducing atoms of Fe into the powders. It is hard to quantify its correct phase percentage in the sample because of its crystallographic and chemical similarity with Co structures, although the profile fit is not well fit without adding it (Fig. S5†). For CoO, one can understand it to be related to air infiltration in the synthesis and its mixture with unreacted Co. Also, ref. 13 detected the presence of CoO by thermal synthesis, showing that it is not only a problem of this kind of synthesis. The presence of CoO is very insignificant, reaching 3% for the 15 h-milled sample.

The α-TeO_2 phase is also present in the initial granular Te reagent as observed in the XRPD measurements (Fig. S6†). The material was easily ground using a mortar and a pestle to increase the XRPD statistics, a process that could provoke a reaction with the air and cause this contamination. The

presence of oxides in the initial reagents also could explain the existence of the CoO. The Te XRPD pattern did not present perfect statistics because of the nature of the material, so the quantification of absolute values obtained there could be imprecise, although α-TeO_2 is present in the sample. Ref. 31 demonstrates that the oxidized reagents may form another composite with mechanical alloying but they do not alter the phase formation of the TMC alloy.

Information about the sample structure and microstructure was obtained through a conventional FPA fit of the diffractogram peaks, furnishing along with it the mass phase percentages evolution presented in Fig. 1(b). Regarding the β-CoTe phase XRPD peaks, no visual difference can be seen in the patterns over time, meaning that it was very stable after 6 h. Fig. 1(c) presents the close-packing ratio (CPR) for the hexagonal structure with milling time, which showed a decrease in the transition from 6 h to 9 h and that stability was reached after then. The occupation factor for the Co atom was refined, which reached values of 0.86 as shown in Fig. 1(d). Fig. 1(e) gives the evolution of the microstructural parameters of β-CoTe with milling time, showing that the average CS decreased a little with milling time and microstrain showed no significant variation, remaining at around 1.1% for milling times over 6 h. So, one can interpret that the physical mechanisms of milling (cold welding, fracturing, and rewelding) are not yet in a steady-state at 15 h of milling.

The β-CoTe phase obtained by mechanochemistry proved to be very stable for 200 days, as shown in Fig. S7.† The XRPD pattern did not change and the same goes for the structural and microstructural parameters, except for a very small variation of the parameters within 77 days, which could be attributed to the method of characterization itself.

The reproducibility of the β-CoTe nanophase synthesized by the novel mechanochemical method was confirmed by preparing a second batch, the XRD pattern of which is shown in Fig. S8.† The phases identified were the same as for the first batch with almost the same β-CoTe phase content and microstructural parameters. The only difference observed was that the Fe and Co reflections were slightly more distinguishable when compared to the first batch.

Table 1 shows a comparison between this work and others regarding the unit cell results. Here, one can see that the CPR is low if compared to the ideal hexagonal structure (1.633), indicating that the crystal structure is composed of atoms more closely packed and loosely connected planes.[13] All works cited present similar c/a values and ours do not diverge. According to M. Schur *et al.*,[13] the shortest Te–Te distance has a value below the sum of two Te^{2-} ionic radii, meaning bonding takes place with these chalcogenides which reduces the CPR.

Also, CoSe[32] was synthesized using the same milling equipment and ball-to-powder ratio, in a different stoichiometry (3 : 1), achieving the $P6_3/mmc$ phase within 72 h of milling, presenting a c/a of 1.53, way higher than this work. Although no occupational factor is refined in this paper, the appearance of this phase for high milling times, in a completely different stoichiometry, can be justified by the high quantity of defects that mechanochemistry can introduce in the sample, thus augmenting the number of vacancies of the Co atoms so characteristic to form these kinds of TMC nickeline structures. With the 1 : 3 stoichiometry[33] for the Co–Se within 3 h of milling, the hexagonal phase could be identified and showed underestimated values for CS of about 7 nm, reaching a mass phase percentage of 60% with 70 h of milling time. Although the chalcogenides changed from Te to Se, the structures seemed to repeat themselves.

3.2. Double-Voigt crystallite size anisotropy modeling

Effective modeling of the size and shape is also possible through the use of a macro for TOPAS developed by J. Neubauer *et al.*[34] This strategy employed the DV approach and used the Lorentzian and Gaussian integral breadths for size parameter calculations, correlating it with the Scherrer equation for mean apparent size. Along with various possible morphologies, here the triaxial ellipsoid shape is used for the CS modeling due to its better agreement. The 15 h-milled sample refinements resulted in the shape presented in Fig. 2, plotted using the Mathematica software[35] and the radii in the figure caption, representing a 'true' CS of 5.249 nm (the cubic root of the volume). These values cannot be compared with the previous results since their definitions are different: the first approach measures the CS diameter mass average and the last uses a surface-weighted average. The R_{wp} value reduced by 0.16% but GoF was reduced by 0.1%, adding just one parameter if compared to the conventional approach.

3.3. Transmission electron microscopy

The microscopy images showed that the crystallites are aggregated into larger nanometric particles with irregular shapes and are of a few hundred nanometers in size. The aggregation of the crystallites took place through the cold-welding mechanism

Table 1 Lattice parameter comparison between other published structures of the β-CoTe phase. Some works use out of stoichiometry phases due to the wide range of homogeneity of this kind of material

Work	Lattice parameter a (Å)	Lattice parameter c (Å)	Volume (Å^3)	Close-packing ratio (c/a)
Ref. 20	3.75–3.88	5.35–5.99	69.05–72.41	1.384–1.606
Ref. 13	3.893	5.371	70.49	1.380
Ref. 14	3.874	5.375	69.86	1.387
Ref. 15	3.85	5.131	65.86	1.33
Ref. 11	3.888	5.378	70.41	1.383
Ref. 16	3.890	5.373	70.41	1.381
This work (15 h-sample)	3.895	5.3809	70.70	1.381

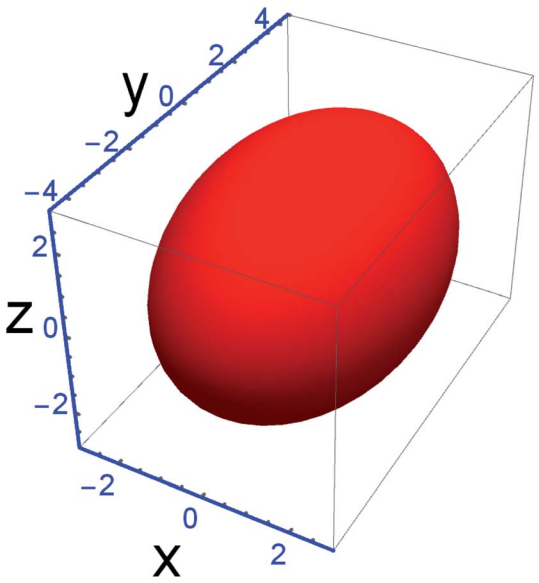

Fig. 2 Crystallite size anisotropy modeled with a triaxial ellipsoid. Values are $r_x = r_z = 2.855$ nm and $r_y = 4.310$ nm. R-values: R_{wp} of 2.78% (R_p 2.11%) and GoF 1.702.

(competing with fracture mechanisms), inherent to the mechanical alloying process. Its visualization is presented in Fig. 3(a) with its magnified portion displayed in Fig. 3(b). These images confirm the particles to have smaller constituents. Using these, one can also measure the CSs according to Fig. 3(c), showing a variety of sizes in the image from 4.6 nm to 15.2 nm. A count using 291 supposed crystallites within 8 pictures furnished the distribution presented in Fig. 4 together with the average and distribution. According to Mittemeijer & Scardi,[36] the number weighted column heights obtained by TEM make a comparison between the Rietveld weight average CS impossible, despite the values being in the same order of magnitude. Also, surface-weighted averages are impossible to match with numerical ones, meaning that the comparison with the above method is not comparable as well. The aggregation could also make it difficult to visualize the CSs and the values for the average size obtained by this technique were probably not very accurate.

In Fig. 3(d), the SAED pattern revealed typical Debye rings that attested to the polycrystalline character of this nanocrystalline material. The Debye ring modeled by JEMS presented an excellent match for the plane spacing retrieved by Rietveld. Only one peak did not correspond to the β-CoTe phase and is presumed to be from the Co or Fe phase due to its location. No CoO was visible in this measurement, probably because of its small quantity in the sample.

3.4. Magnetic measurements and simulation results

The descending branches of the magnetization hysteresis loops, obtained through VSM at 300 K for the $Co_{50}Te_{50}$ samples with different milling times, are displayed in Fig. 5. Fig. S9† also shows these loops for the 15 h-milled sample, together with their temperature variations measured down to 10 K *via* PPMS.

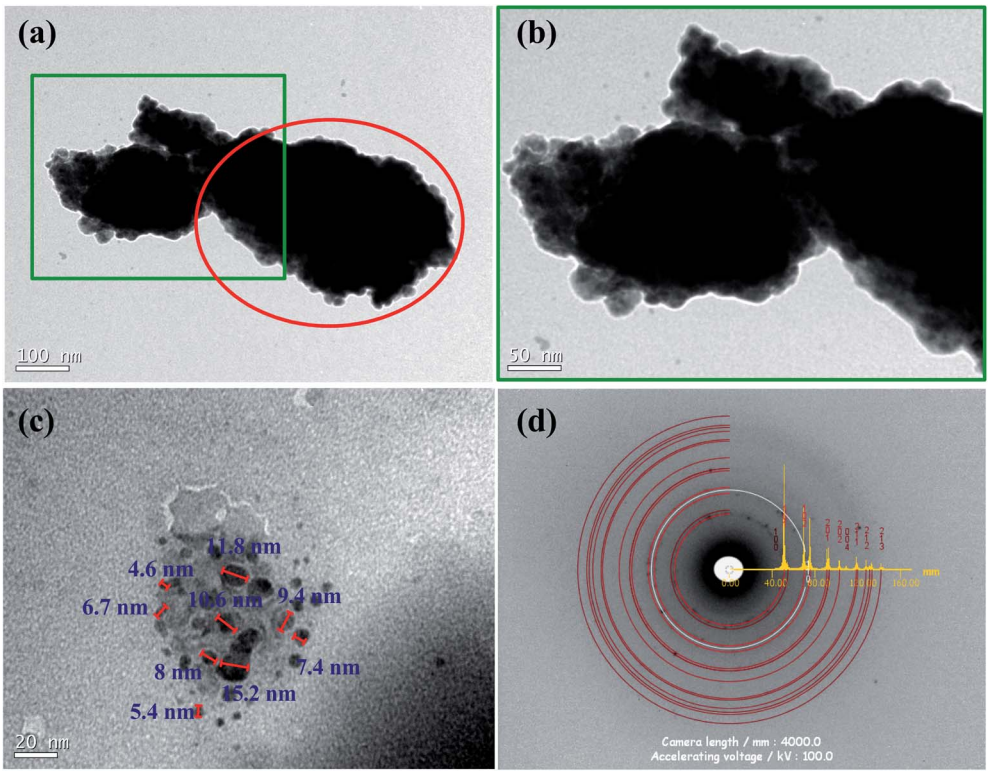

Fig. 3 (a) TEM 100 kV image of the $Co_{50}Te_{50}$ milled for 15 h. (b) Magnified image corresponding to the green square. (c) Another picture from the sample showing the crystallite sizes. (d) SAED measurements modeled with JEMS. The white ring was fitted for the Co/Fe phase, and the red rings represent the β-CoTe. The *hkl*s of each peak are above them.

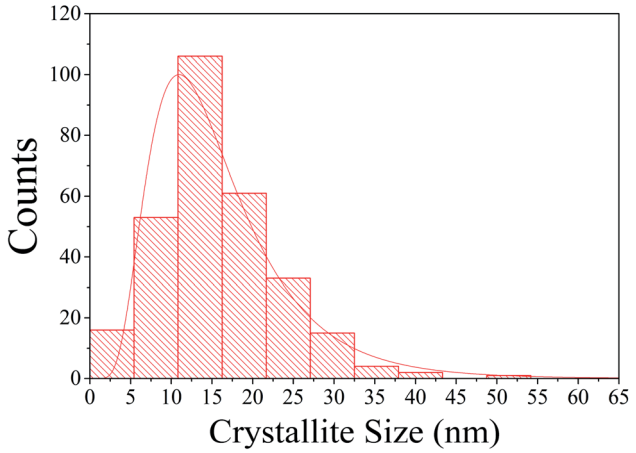

Fig. 4 Histogram of CS counts in the TEM images for the 15 h-milled sample and its fit according to a log-normal distribution. The average was 16 nm with a standard deviation of 8.7 nm. The number of crystallites used was 291 with sizes varying from 2 nm to 53 nm. The boxes' sizes used 5.4 nm of width.

Although all curves exhibit some hysteresis (a small yet nonzero remnant magnetization and coercivity, H_C), these certainly present features characteristic of disordered systems consisting of predominantly superparamagnetic (SPM) grains *i.e.*, at sufficiently high temperatures, their magnetizations are thermally agitated, allowing them to rotate away from the respective equilibrium directions and towards that of H. The average size, $\langle d \rangle$, of the SPM particles and the sample's saturation magnetization, M_S, are obtained by fitting the experimental magnetization curves taking into account both ferromagnetic (FM) and SPM contributions.[37,38] Given that each fitting curve is a superposition of the SPM and FM parts, the method also yields the coercivity value of the FM phase, H_C^{FM}.

Fig. 6 shows the three parameters, $\langle d \rangle$, M_S and H_C^{FM}, obtained from the simulations for different milling times of $Co_{50}Te_{50}$ at 300 K, and for different measurement temperatures for the 15 hour milled sample (the value of the other parameter used, *i.e.*, the width of the log-normal grain-size distribution, was kept constant, equal to 1.5). The majority of these parameters present monotonous variations with both milling time and temperature, except for $\langle d \rangle$ and M_S as functions of the milling time. The value of $\langle d \rangle$ increased by ~53% and that of M_S decreased by ~67% from 3 h to 9 h of milling. For greater milling times, $\langle d \rangle$ and M_S present a weak gradual decrease, while H_C^{FM} steadily reduces with the milling time, where more than twofold shrinking from 3 h to 15 h was estimated. All these parameters vary monotonously with the measurement temperature. However, while H_C^{FM} decreases exponentially, $\langle d \rangle$ and M_S change in a linear manner – a small decrease of M_S and an increase of $\langle d \rangle$.

The variation of $\langle d \rangle$ with T can be understood by bearing in mind that $\langle d \rangle$, estimated from our magnetization curves' fittings, represents a "magnetic" size, *i.e.*, that of an entity which is SPM at the measurement conditions. Very small interacting grains tend to agglomerate, which is also facilitated by thermal agitation at higher temperatures where only great (polycrystalline with weak magnetic anisotropy) clusters are FM, contributing to H_C^{FM}. With the decrease of T, the number of magnetically-frozen grains with smaller $\langle d \rangle$ and stronger anisotropy (and thus higher H_C^{FM} values) increases, reflected in the great increase of H_C^{FM} when T decreases.

A ZFC/FC pair of curves, measured upon application of a magnetic field of 100 Oe, was traced for the $Co_{50}Te_{50}$ 15 h-milled sample, for temperatures ranging between 5 K and 300 K (Fig. S10†). Due to the H-value being much lower than the system's anisotropy field at 300 K (estimated to be of ~3 kOe), there is significant splitting between the FC and ZFC curves, there is no temperature region with reversible magnetization rotation as well as no indication to the existence of the SPM blocking temperature.

As seen in Fig. 6 and S9,† there is good agreement between model and experiment, indicating rather weak or absent FM intergrain interactions. For their evaluation, we employed the recently-developed δM_R interaction plots technique.[39] The method is based on measuring a recoil loop, where H is cycled

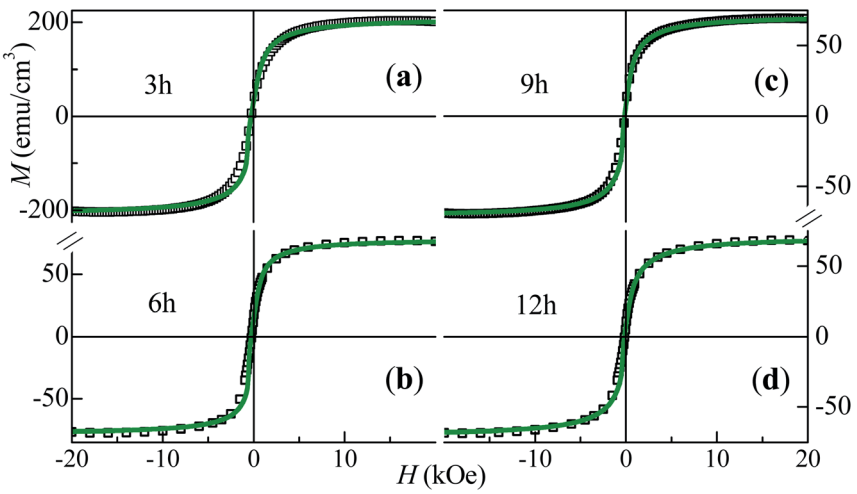

Fig. 5 Symbols: descending branches of the $M \times H$ loops obtained at 300 K *via* VSM measurements for $Co_{50}Te_{50}$ with different milling times; the lines are the respective fitting curves.

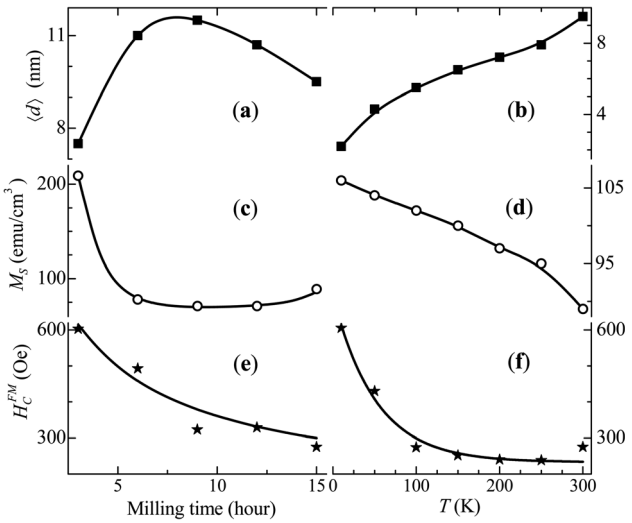

Fig. 6 Parameters estimated from the magnetization hysteresis loops' simulations for different milling times of $Co_{50}Te_{50}$ (left panels) at 300 K and for different measurement temperatures (right panels) for the 15 hour milled sample. Panels (a) and (b): the mean size of the SPM part of each sample; (c) and (d): total saturation magnetization; (e) and (f): coercive field of the respective ferromagnetic part. The lines are merely guides for the eye.

between the maximum positive magnetic field and a smaller field, called recoil field, H_R. Here, we constructed δM_R plots for recoil loops with $H_R \cong H_C$, traced at 300 K for the samples with different milling times. These plots, each normalized to the value of M obtained at $H = 18$ kOe of the respective recoil loops, are shown in Fig. 7. For $H \lesssim 4$ kOe, all $\delta M_R(H)$ values exhibit negative deviations which, in uniaxial-anisotropy systems, are normally ascribed to a dipolar-like behaviour, stabilizing the demagnetized magnetic coupling state. However, the inset of Fig. 7 reveals these interactions in our system to be very weak, given the very small δM_R amplitude value as compared to the major loop

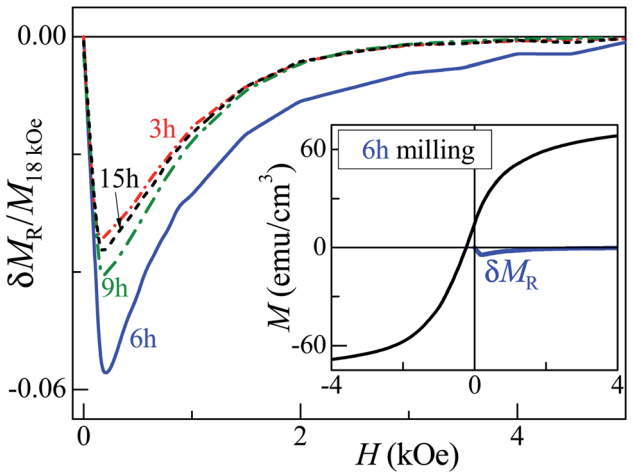

Fig. 7 δM_R interaction plots, obtained from recoil loops with recoil fields equal to the respective coercive field value at 300 K, of $Co_{50}Te_{50}$ samples for different ball-milling times. The inset gives the δM_R plot with the greatest amplitude together with the descending branch of the corresponding major loop.

magnetization (theoretically, the amplitude of such a plot may reach a value twice as high as M_S). Thus, our analysis reveals that the coupling between the FM grains is practically negligible, *i.e.*, their aggregation is insignificant. It is worth mentioning that the FM contribution could also be related to the presence of a small amount of elemental Fe, Co or CoO in the samples.

4. Conclusions

The β-CoTe phase was synthesized successfully by the mechanical alloy of pure elemental reagents, using a single-step procedure that resulted in 93% of its mass phase percentage after 6 h of milling. The reproducibility and stability of the β-CoTe nanophase were verified and attested. TEM and XRPD results showed the crystals to be nanometric in size with TEM recording an average of 16 nm in diameter and a mass diameter average of about 13 nm being retrieved by the Rietveld FPA. The DV anisotropy approach for the CSs resulted in a surface-weighted 'true' CS average of 5.2 nm using a triaxial ellipsoid shape for modeling. No comparison between these numbers was possible due to their different nature. The values of the close-packing ratio proved to be smaller if compared to the ideal hexagonal structure but agreed with literature values. The occupational factor refinement revealed 86% of site occupancy for Co. Future studies should be produced to check for the suitable mechanochemistry stoichiometry that forms a pure phase for β-CoTe. Numerical simulations allowed us to estimate the average size of the SPM (β-CoTe phase) particles and the sample's saturation magnetization M_S by fitting the experimental magnetization curves, also taking into account the ferromagnetic contribution.

Conflicts of interest

There are no conflicts to declare.

Acknowledgements

We are grateful to the Brazilian agencies CNPq (grants 421747/2016-1, 310175/2016-0, 305796/2016-0, and 150535/2019-8) and CAPES (M. A. M. Master and K. F. U. PhD Scholarships) for financial support. The XRPD, VSM and TEM/SAED/EDS measurements were performed at Laboratório de Difração de Raios-X (LDRX), Laboratório Multiusuário de Caracterização Magnética de Materiais (LabCAM) and Laboratório Central de Microscopia Eletrônica (LCME) multiuser facilities at UFSC.

References

1 R. R. Chianelli, *et al.*, Catalytic properties of single layers of transition metal sulfide catalytic materials, *Catal. Rev.: Sci. Eng.*, 2006, **48**, 1–41.
2 C.-A. Tseng and C.-P. Lee, Transition Metal Chalcogenides for the Electrocatalysis of Water, *IntechOpen*, 2020, **38**, DOI: 10.5772/intechopen.92045.
3 H. Yuan, L. Kong, T. Li and Q. Zhang, A review of transition metal chalcogenide/graphene nanocomposites for energy storage and conversion, *Chin. Chem. Lett.*, 2017, **28**, 2180–2194.

4 N. Balis, E. Stratakis and E. Kymakis, Graphene and transition metal dichalcogenide nanosheets as charge transport layers for solution processed solar cells, *Mater. Today*, 2016, **19**, 580–594.
5 D. Jariwala, V. K. Sangwan, L. J. Lauhon, T. J. Marks and M. C. Hersam, Emerging device applications for semiconducting two-dimensional transition metal dichalcogenides, *ACS Nano*, 2014, **8**, 1102–1120.
6 L. Takacs, The historical development of mechanochemistry, *Chem. Soc. Rev.*, 2013, **42**, 7649–7659.
7 C. Suryanarayana, *Mechanical alloying and milling*, 2004, vol. 46, pp. 1–472.
8 P. Baláž, M. Baláž, M. Achimovičová, Z. Bujňáková and E. Dutková, Chalcogenide mechanochemistry in materials science: insight into synthesis and applications (a review), *J. Mater. Sci.*, 2017, **52**, 11851–11890.
9 H. Yuan, *et al.*, Thermodynamic assessment of the Te-X (X = As, Si, Co) systems, *Calphad*, 2020, **68**, 101743.
10 T. A. Bither, R. J. Bouchard, W. H. Cloud, P. C. Donohue and W. J. Siemons, Transition Metal Pyrite Dichalcogenides. High-Pressure Synthesis and Correlation of Properties, *Inorg. Chem.*, 1968, **7**, 2208–2220.
11 P. d. M. d. Betzembroeck and J. Naud, Étude par diffraction-X de quelques composés du système Ni-Co-Te obtenus par synthèse thermique, *Bull. Soc. Chim. Belg.*, 1971, **80**, 107–116.
12 R. M. Geffken, K. L. Komarek and E. M. Miller, Thermodynamic properties of cobalt-tellurium alloys, *J. Solid State Chem.*, 1972, **4**, 153–162.
13 M. Muhler, W. Bensch and M. Schur, Preparation, crystal structures, experimental and theoretical electronic band structures of cobalt tellurides in the composition range $CoTe_{1.3}$-$CoTe_2$, *J. Phys.: Condens. Matter*, 1998, **10**, 2947–2962.
14 H. Schicketanz, P. Terzieff and K. L. Komarek, Thermoelectric and Magnetic Measurements on polycrystalline and single-crystal $Co_{1-x}Te$, *J. Less-Common Met.*, 1986, **119**, 13–20.
15 B. R. Dahal, R. P. Dulal, I. L. Pegg and J. Philip, Ferrimagnetic $Co_{1+\delta}Te$ nanostructures, *Mater. Res. Express*, 2016, **3**, 1–6.
16 K. O. Klepp and K. L. Komarek, Übergangsmetall-Chalkogensysteme, 4, Mitt.: Die systeme Kobalt-Tellur und Kobalt-Nickel-Tellur, *Monatsh. Chem.*, 1973, **104**, 105–117.
17 S. Pradhan, *et al.*, Chemical synthesis of nanoparticles of nickel telluride and cobalt telluride and its electrochemical applications for determination of uric acid and adenine, *Electrochim. Acta*, 2017, **238**, 185–193.
18 K. de Fatima Ulbrich, J. P. Winiarski, C. L. Jost and C. E. M. de Campos, Green and facile solvent-free synthesis of $NiTe_2$ nanocrystalline material applied to voltammetric determination of antioxidant morin, *Mater. Today Commun.*, 2020, **25**, 101251.
19 K. de Fatima Ulbrich, J. P. Winiarski, C. L. Jost and C. E. Maduro de Campos, Mechanochemical synthesis of a $Ni_{3-x}Te_2$ nanocrystalline composite and its application for simultaneous electrochemical detection of dopamine and adrenaline, *Composites, Part B*, 2020, **183**, 107649.
20 M. S. Khan, M. N. Ashiq, M. F. Ehsan, T. He and S. Ijaz, Controlled synthesis of cobalt telluride superstructures for the visible light photo-conversion of carbon dioxide into methane, *Appl. Catal., A*, 2014, **487**, 202–209.
21 Y. He, *et al.*, Review Of Nanoscale Layered Transition Metal Chalcogenide Superconductors, *Adv. Mater. Lett.*, 2019, **10**, 152–163.
22 D. Ectors, F. Goetz-Neunhoeffer and J. Neubauer, Domain size anisotropy in the double-Voigt approach: an extended model, *J. Appl. Crystallogr.*, 2015, **48**, 1998–2001.
23 Bruker AXS, *TOPAS*, 2009.
24 K. F. Ulbrich and C. E. M. Campos, Stability of iron selenide nanophases prepared by mechanosynthesis, *AIP Adv.*, 2019, **9**, 045311.
25 K. F. Ulbrich, *et al.*, A comprehensive structural and microstructural investigation of a new iron-telluride nano phase, *J. Mater. Chem. C*, 2018, **6**, 3047–3057.
26 K. F. Ulbrich and C. E. M. Campos, Nanosized tetragonal β-FeSe phase obtained by mechanical alloying: structural, microstructural, magnetic and electrical characterization, *RSC Adv.*, 2018, **8**, 8190–8198.
27 I. Levin, *NIST Inorganic Crystal Structure Database (ICSD)*, 2018, DOI: 10.18434/M32147.
28 G. Hölzer, M. Fritsch, M. Deutsch, J. Härtwig and E. Förster, Kα1,2 and Kbeta1,3 x-ray emission lines of the 3d transition metals, *Phys. Rev. A: At., Mol., Opt. Phys.*, 1997, **56**, 4554–4568.
29 D. Black, D. Windover and A. Henins, Standard reference material 660b for X-ray metrology, *Adv. X-Ray Anal.*, 2009, 140–148.
30 *JEMS, v 4*, Switzerland.
31 C. E. M. Campos, *et al.*, Influence of minor oxidation of the precursor powders to form nanocrystalline CdTe by mechanical alloying, *J. Alloys Compd.*, 2008, **466**, 80–86.
32 C. E. M. Campos, J. C. D. Lima, T. A. Grandi, K. D. Machado and P. S. Pizani, Structural studies of cobalt selenides prepared by mechanical alloying, *Phys. Rev. B: Condens. Matter Mater. Phys.*, 2002, **324**, 409–418.
33 C. E. M. d. Campos, *Estudo De Propriedades Físicas De Nanomateriais Produzidos Por Síntese Mecânica*, Universidade Federal de Santa Catarina, 2005.
34 D. Ectors, F. Goetz-Neunhoeffer and J. Neubauer, A generalized geometric approach to anisotropic peak broadening due to domain morphology, *J. Appl. Crystallogr.*, 2015, **48**, 189–194.
35 Wolfram Research, *I. Mathematica*, 2020.
36 A. Kern, A. A. Coelho and R. W. Cheary, Convolution based profile fitting, *Diffraction Analysis of the Microstructure of Materials*, ed. E. J. Mittemeijer and P. Scardi, Materials Science, Springer, 2004, pp. 17–50, ISBN 3-540-40510-4; Bruker, *Topas 5 Technical Reference Manual*, 2014.
37 A. D. C. Viegas, J. Geshev, L. S. Dorneles and J. E. Schmidt, Correlation between magnetic interactions and giant magnetoresistance in melt-spun $Co_{10}Cu_{90}$ granular alloys, *J. Appl. Phys.*, 1997, **82**, 3047–3053.
38 V. Masheva, *et al.*, On the magnetic properties of nanosized $CoFe_2O_4$, *J. Magn. Magn. Mater.*, 1999, **196**, 128–130.
39 J. Geshev, Interaction plots obtained from in-field magnetization instead of remanence measurements, *J. Magn. Magn. Mater.*, 2018, **467**, 135–138.